A 6–32.5 GHz Gain-Enhanced and Harmonically Tuned Class-E SiGe Cascode Power Amplifier with 19.2 dBm Peak $\mathrm{P_{SAT}}$ and 34% Peak PAE

Eren Vardarli[#1], Austin Ying-Kuang Chen[$], Paulius Sakalas[#], Michael Schröter[#]
[#]Chair for Electron Devices and Integrated Circuits, TU Dresden, 01062 Dresden, Germany
[$]Department of Electrical and Computer Engineering, University of California, Santa Cruz, USA
[1]eren.vardarli@tu-dresden.de

***Abstract*— This paper presents an ultra-wideband (UWB) class-E SiGe cascode power amplifier (PA) which features a 3 dB small-signal bandwidth (BW) of 138% (6–32.5 GHz) and a 1 dB large-signal power BW of 132% (7–34 GHz), targeting SATCOM, 5G/B5G, and emerging 6G applications. At 14 GHz, the PA demonstrates a measured peak $\mathrm{P_{SAT}}$ and $\mathrm{OP_{1dB}}$ of 19.2 dBm and 17.8 dBm, respectively. At 28 GHz, the PA achieves a measured $\mathrm{P_{SAT}}$/$\mathrm{OP_{1dB}}$ of 18.5/17 dBm, a power gain of 23.5 dB, with a 3 dB gain peaking attributed to the second-order LC low-pass filter (LPF) embedded in the output load network (OLN). In addition, a harmonically tuned OLN incorporating a quarter-wave transformer (QWT) is employed to enhance efficiency over the wide BW, resulting in a measured PAE of >28% from 8 to 31 GHz, with a peak PAE of 34% at 28 GHz. Tested with a single-carrier 400 MHz 64-QAM DFT-s-OFDM modulated signal, the PA delivers a $\mathrm{P_{avg}}$/$\mathrm{PAE_{avg}}$ of 15.5 dBm/16.3% with an excellent EVM of -28.6 dB at 28 GHz, supporting a data rate up to 2.4 Gbps. To the best of the authors' knowledge, this class-E PA achieves the widest BW with excellent FoM, PAE, and linearity performance among all previously published silicon-based wideband PAs to date.**

***Keywords*— 5G/B5G, 6G, ACLR, EVM, millimeter-wave, multiband, PA, PAE, SiGe BiCMOS, ultra-wideband.**

I. INTRODUCTION

Very high throughput satellite (VHTS) communications in low Earth orbit (LEO) are transitioning from lower microwave bands (L/S/C) to higher frequency bands (X/Ku/K/Ka) to accommodate growing demands for increased data capacity and reduced latency [1], [2]. These systems rely on high-element-count phased arrays with multiple dedicated RF transmitters, necessitating highly efficient PAs that minimize DC power consumption while delivering sufficient gain and output power [3], [4]. In addition, 5G millimeter-wave (mm-wave) bands (n257, n258, n261), which operate within the K- and Ka-bands, impose stringent peak-to-average power ratio (PAPR) requirements, driving the need for PAs optimized for both linearity and efficiency under power back-off (PBO) conditions [5]. Furthermore, the emerging 6G mobile communication standard is considering a new frequency range (FR3) from 7 to 15 GHz (spanning the X- and Ku-bands), reinforcing the demand for advanced multiband PAs that can meet these diverse and evolving requirements.

In this work, we present an ultra-wideband, high-efficiency class-E SiGe PA that incorporates a second-order LC LPF for passive gain enhancement and QWT for harmonic tuning. These design techniques significantly improve large-signal performance, enabling quad-band operation across X/Ku/K/Ka-bands for SATCOM, 5G/B5G, and emerging 6G applications. The circuit was fabricated in SG13G2Cu, a 0.13 µm BiCMOS production technology of IHP Microelectronics which features six copper and two aluminum metal layers. The high-speed npn device achieves a peak $f_\mathrm{T}/f_\mathrm{max}$ of 350/450 GHz at the collector current density (J_C) of $\sim$23 $\mathrm{mA/\mu m^2}$.

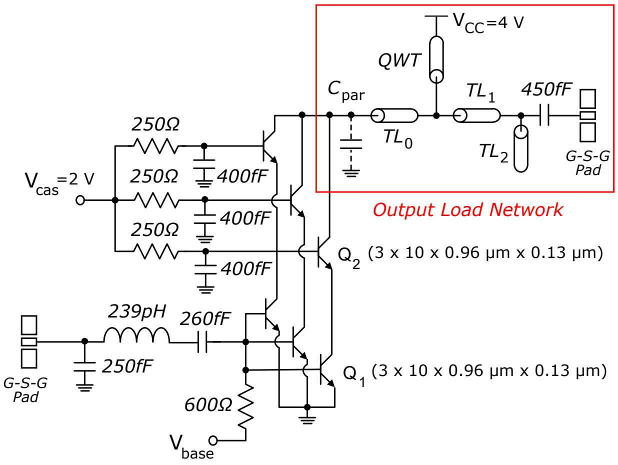

Fig. 1. Schematic of the ultra-wideband class-E cascode PA.

II. CIRCUIT DESCRIPTION AND DESIGN CONSIDERATIONS

The schematic of the ultra-wideband class-E cascode PA is shown in Fig. 1 where the OLN is composed of TL_0, TL_1, TL_2, QWT, parasitic capacitance (C_par) of Q_2, series output capacitance (C_out), and pad capacitance (C_pad). To achieve a target $\mathrm{P_{SAT}}$ of $\sim$20 dBm, the common-base (CB) and common-emitter (CE) stages of the cascode are configured with three HBTs connected in parallel where each HBT has the maximum number of parallel unit cells of ten, resulting in a total emitter area (A_E) of 3.744 $\mathrm{\mu m^2}$. Further increase in A_E has been avoided to limit C_par and thus achieve optimal class-E operation.

The detailed TL-based OLN is illustrated in Fig. 2a. The 2$^\mathrm{nd}$-order LC LPF is synthesized with TL_1 and TL_2 which provides a sharp rolloff of -40 dB/dec for harmonic filtering at the output. To realize gain enhancement and BW extension, the quality factor of the LC LPF is designed to achieve a damping coefficient (ζ) <1, resulting in an underdamped response, which provides the 3 dB gain peaking at 28 GHz. The LPF also serves as the matching network to transform

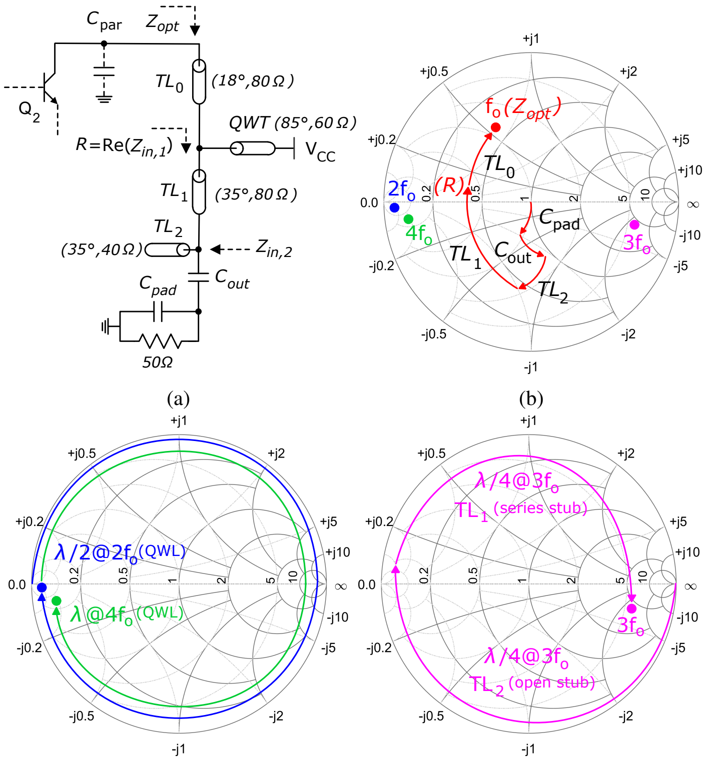

(a) (b)

(c) (d)

Fig. 2. (a) TL-based output network of the class-E cascode PA and simulated harmonic impedance trajectories at (b) f_0, (c) $2f_0$ and $4f_0$, (d) $3f_0$.

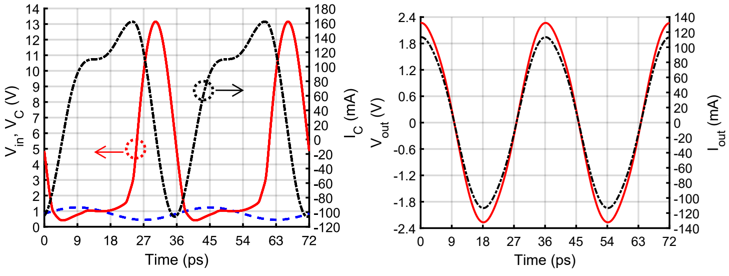

(a) (b)

Fig. 3. (a) Simulated V_{C}, I_{C} of Q_2 and the input voltage (blue dashed) at the base of Q_1. (b) Output voltage across (red solid) and current (black dashed-dotted) through the load impedance of $50\,\Omega$ at $\mathrm{OP}_{1\mathrm{dB}}$ and 28 GHz.

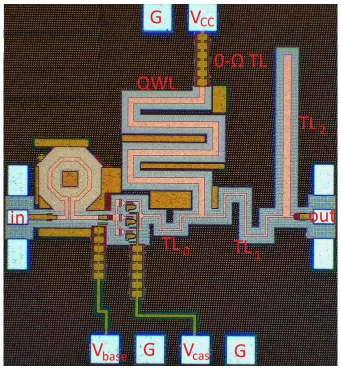

Fig. 4. Chip micro-photograph of the ultra-wideband class-E cascode PA.

$50\,\Omega$ load to optimum impedance (Z_{opt}) and provides the necessary open-circuit condition for the voltage waveform at 3rd harmonic.

TL_0 represents the series inductance L which isolates the collector node from the QWT and prevents 2nd harmonic short, thereby improving efficiency. Together with C_{par}, it is also used to tune the collector node at a frequency higher than the fundamental ($f_0 = 28$ GHz), which produces non-sinusoidal and thus non-overlapping class-E voltage and current waveforms. These waveforms ensure zero voltage switching (ZVS) and zero voltage derivative switching (ZVDS) conditions needed for class-E operation. As shown in Fig. 2a, Z_{opt} seen looking into TL_0 is given by

$$Z_{opt} \approx Z_{in,1} + jZ_0 \tan(\theta_0) \approx R + jZ_0 \tan(\theta_0), \qquad (1)$$

where $Z_{in,1}$ is the load impedance seen by TL_0 which should be equal to the optimum resistance ($R = 19\,\Omega$) found from class-E network equations [6]. Using the class-E network equation for L at $q = 1/(\omega_0 \cdot L \cdot C_{par}) = 1.64$ (tuning factor), where $\mathrm{Im}(Z_{opt}) = Z_0 \tan(\theta_0) = \omega_0 L$, θ_0 is given as

$$\theta_0 = \arctan(1.371 \cdot \frac{R}{Z_0}). \qquad (2)$$

Targeting a Z_0 value of $80\,\Omega$ by employing a narrow width for TL_0, θ_0 is found as 17.6 °.

The impedance trajectories at f_0 and higher-order harmonics ($2f_0$, $3f_0$, $4f_0$) are illustrated in Fig. 2. Both C_{pad} and C_{out} contribute to the synthesis of Z_{opt} at f_0, which provides additional design freedom to achieve the desired matching and gain peaking simultaneously, as shown in Fig. 2b. Fig. 2c illustrates the impedance trajectories at $2f_0$ and $4f_0$ where the equivalent length of the QWT is $\lambda/2$ and λ, respectively, effectively AC-grounding the signal. This desired short-circuit condition improves the linearity performance by further reducing even-order harmonic and odd-order intermodulation distortion products. Fig. 2d depicts the trajectory at $3f_0$, where TL_2 performs open to short transformation since it is a QWT at this harmonic. Starting from $Z_{in,2}$, TL_1 completes the high impedance transformation that trap $3f_0$ at the collector, thereby enhancing efficiency.

The ZVS and ZVDS conditions can be validated from Fig. 3a where the collector voltage (V_{C}) and its derivative/slope reaches its minimum value when the HBT turns on and the collector current (I_{C}) becomes positive at around 40 ps. The non-ideal turn-off behavior of the HBT and the corresponding negative I_{C} indicate the charging and the discharging of C_{par} at the collector node during the off-cycle. It is worth noting that V_{max} is reached when the collector node is fully charged and the current going into the node becomes zero (i.e., $I_{\mathrm{C}} = 0$). From this point on, I_{C} is negative (i.e. going out of the node) and the nodal capacitance is being discharged until it reaches the minimum point before the HBT turns on, satifying ZVS and ZVDS.

III. MEASUREMENT SETUP AND EXPERIMENTAL RESULTS

The micro-photograph of the PA is shown in Fig. 4. The overall chip area including the pads is 0.9 mm x 0.98 mm. All components including the metal stacks, input/output networks, pads, and 0-Ω TLs were EM-simulated using the 2.5D

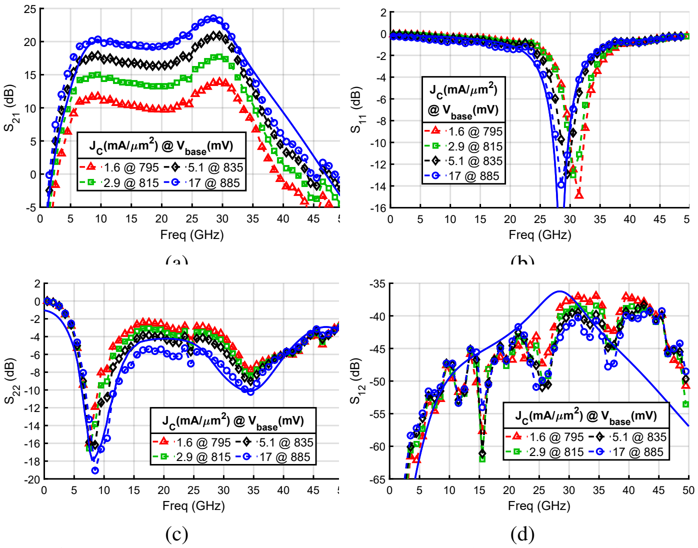

(a) (b)

(c) (d)

Fig. 5. Measured S-parameters at various J_{C} for $V_{\mathrm{CC}} = 4\,\mathrm{V}$ and $V_{\mathrm{cas}} = 2\,\mathrm{V}$ (blue solid line represents the simulated results at $17\,\mathrm{mA/\mu m^2}$).

ADS Momentum. The small-signal measurements of the PA were performed using 1.85 mm coaxial cables, DC-67 GHz GSG Z-probes from FormFactor and the 4-port N5245B PNA-X (10 MHz-50 GHz). An on-wafer SOLT calibration was performed using ISS (101-190 C) to bring the reference plane to the tip of the RF probes. The large-signal power sweeps including AM-PM were measured using the same setup with measurement class options installed within the PNA-X. For EVM and adjacent channel leakage ratio (ACLR) measurements, 5G NR FR2 compliant I/Q waveforms were generated with the M9484C VXG vector signal generator and was analyzed using N5245B PNA-X with modulation distortion class.

The measured S-parameters of the PA are shown in Fig. 5 for various J_{C}. At $17\,\mathrm{mA/\mu m^2}$ (light class AB bias), the PA achieves a peak gain of 23.5 dB at 28 GHz, along with a very wide 3 dB small-signal BW of 138% (from 6 to 32.5 GHz), partly attributed to passive gain enhancement (Fig. 5a). At deeper class-AB biases, i.e., 5.1, 2.9, $1.6\,\mathrm{mA/\mu m^2}$, the measured gain at 28 GHz is 21.5, 17.5, and 14 dB, respectively. As shown in Fig. 5b and Fig. 5c, the input return loss ($|\mathrm{S}_{11}|$) is 14 dB at 28 GHz while the output return loss ($|\mathrm{S}_{22}|$) is ≥ 6 dB from 5 to 40 GHz at $17\,\mathrm{mA/\mu m^2}$. The OLN provides dual output conjugate impedance matching at 8 and 35 GHz to achieve quad-band performance. The PA is unconditionally stable, with reverse isolation ($|\mathrm{S}_{12}|$) better than 35 dB under all bias conditions and across the frequencies of interest, as shown in Fig. 5d.

Fig. 6a depicts the measured power gain and the PAE versus the output power at $17\,\mathrm{mA/\mu m^2}$ where various critical frequencies for VHTS, 5G FR2, and 6G FR3 are provided. At 14 GHz, the PA demonstrates a highest $\mathrm{P_{SAT}}$ and $\mathrm{OP_{1dB}}$ of 19.2 dBm and 17.8 dBm, respectively. The PA achieves a measured $\mathrm{P_{SAT}}/\mathrm{OP_{1dB}}$ of 18.5/17 dBm at 28 GHz, while maintaining a $\mathrm{P_{SAT}}$ of >16.9 dBm from 7 to 34 GHz (Fig. 6b), demonstrating an exceptionally wide 1 dB large-signal power bandwidth of 132%. The worst-case measured AM-PM distortion of the PA up to $\mathrm{OP_{1dB}}$ is -6°, -2.5°, 1°, 0°, and 3° at 10, 14, 18, 22, and 28 GHz, respectively. Fig. 6b also illustrates the measured peak PAE which is >28% from 8 to 31 GHz and reaches 34% at 28 GHz, due in part to the additional 3 dB gain enhancement. The measured PAE at $\mathrm{OP_{1dB}}$ is 22.6 %, 19.6 %, 19.3 %, 19.7 %, and 23.6 % at 10, 14, 18, 22 and 28 GHz, respectively. Excellent model-to-hardware correlation is achieved through extensive EM simulation and the compact HBT model HICUM/L2 [7]. For device reliability, the PA is tested with continuous-wave power at $\mathrm{OP_{1dB}}$ for 120 hours without noticeable performance degradation.

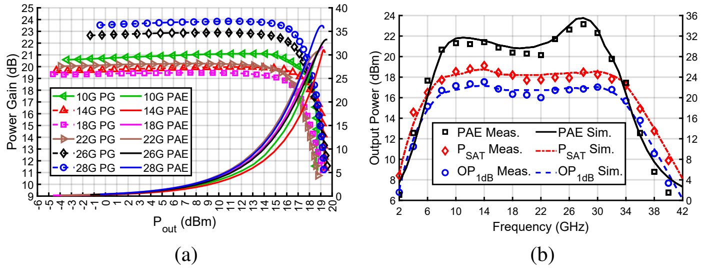

(a) (b)

Fig. 6. (a) Measured power gain and PAE versus $\mathrm{P_{out}}$ at $f_0 = 10\,\mathrm{GHz}$, 14 GHz, 18 GHz, 22 GHz, 26 GHz, and 28 GHz. (b) Measured and simulated $\mathrm{P_{SAT}}$, $\mathrm{OP_{1dB}}$, and peak PAE.

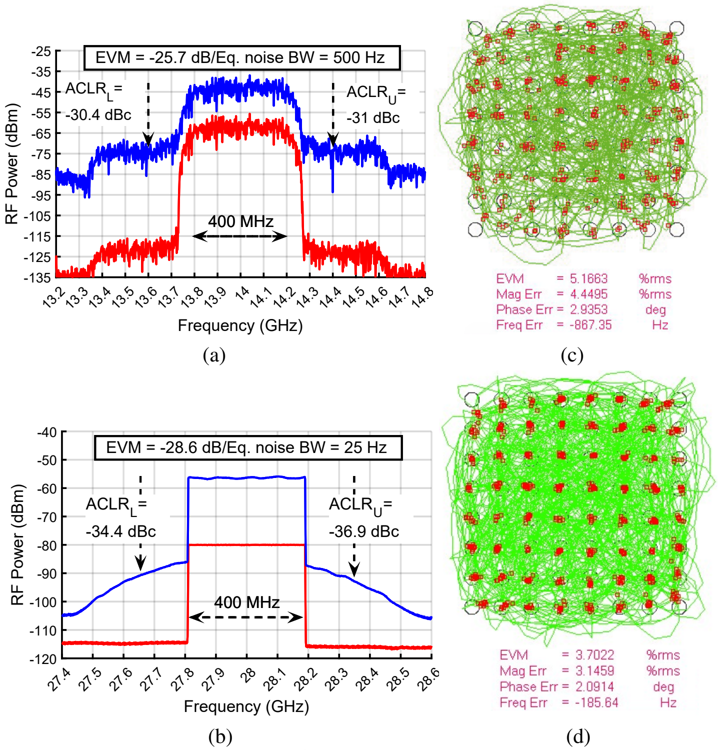

(a) (c)

(b) (d)

Fig. 7. Measured modulated (64-QAM) input (red) and output (blue) spectrum with a signal BW of 400 MHz at (a) 14 GHz (RRC) and (b) 28 GHz (DFT-s-OFDM). Corresponding measured constellation diagrams at (c) 14 GHz and (d) 28 GHz.

Fig. 7 shows the linearity characteristics of the PA at 14 GHz using root-raised cosine (RRC) pulse shaping (rolloff factor = 0.35), and at 28 GHz using a single-carrier 400 MHz 64-QAM DFT-s-OFDM with a sub-carrier spacing of 120 kHz. At 14/28 GHz, the measured ACLR and EVM are better

Table 1. Comparison of State-of-the-Art Ka-band Silicon-based PAs without Power Combining.

Ref.	Tech.	$f_\mathrm{T}/f_\mathrm{max}$ (GHz)	Topology	Freq. (GHz)	$\mathrm{P_{SAT}}$ (dBm)	$\mathrm{OP_{1\,dB}}$ (dBm)	$\mathrm{P_{SAT}}$-1dB BW (GHz)	Gain (dB)	Peak PAE (%)	Mod. Scheme Signal BW (MHz)	EVM (dB)	$\mathrm{P_{avg}}$ / $\mathrm{PAE_{avg}}$ (dBm / %)	FoM^a
[8]	28 nm CMOS	410/230	diff. 2-stage CS^b	28	18.9	18.5	27^c to 30^c	18.5	39.7	64-QAM OFDM 720	-25.4	9.3/10.3	25.4
[9]	45 nm SOI CMOS	290/410	diff. 2-stage class-F/F^{-1} CS	28	18.9	16.9	23 to 40.5	18.7	43.2	64-QAM 1-CC 500	-28.1	10.3/13.1	28.6
[10]	65 nm CMOS	180/330	diff. CS + diff. 3-stacked	29	22.7	22.4	27^c to 30^c	25.2	25.8	64-QAM 100	-25	15.6/13^c	31
[11]	130 nm SiGe:C	350/450	diff. CAS^d	28	22.7	22.1	26^c to 30^c	19.4	38.1	64-QAM 800	-25.2	16.2/11	25.3
[12]	130 nm SiGe	260/350	CE + diff. CAS	28	22.6	21.6	24 to 32	26.5	40.3	64-QAM OFDM 400	-25	15.6/16.3	37.8
This work	**130 nm SiGe:C**	**350/450**	**CAS class-E w/ 2$^{\mathrm{nd}}$-order LPF**	**14** **28**	**19.2** **18.5**	**17.8** **17**	**7 to 34**	**19.7** **23.5**	**30.8** **34**	**64-QAM RRC/OFDM 400**	**-25.7** **-28.6**	**16.2/13.8** **15.5/16.3**	**26.5** **33**

$$^a\mathrm{FoM} = \mathrm{P_{SAT}(dBm)} + \mathrm{Gain(dB)} + 20 \cdot \log\left(\frac{\mathrm{Freq.\ (GHz)}}{f_\mathrm{max}\,\mathrm{(GHz)}}\right) + 10 \cdot \log\left(\frac{\mathrm{BW_{1\,dB}\ (GHz)}}{\mathrm{Freq.\ (GHz)}}\right) + 10 \cdot \log\left(\mathrm{PAE(\%)}\right)$$

^{b}CS = common-source, ^{c}estimated from plot, ^{d}CAS = cascode

than -30.4/-34.4 dBc and -25.7/-28.6 dB, respectively, at 3 dB PBO, as shown in Fig. 7a to Fig. 7d. Correspondingly, the PA delivers a measured $\mathrm{P_{avg}}$ of 16.2/15.5 dBm and a $\mathrm{PAE_{avg}}$ of 13.8/16.3% at 14/28 GHz, respectively, while supporting data rate up to 2.4 Gbps.

Table 1 outlines the performance of this work and other previously published state-of-the-art silicon-based Ka-band PAs without power combining [8]–[12]. This work demonstrates the widest 1 dB large-signal and 3 dB small-signal BWs while delivering excellent linearity and PAE performance using the passive gain-enhancement and harmonic tuning techniques. An additional frequency point (14 GHz) is provided to benchmark the emerging 6G FR3 where the PA shows an excellent $\mathrm{P_{avg}}$ of 16.2 dBm with an EVM of -25.7 dB when tested with a single-carrier 400 MHz 64-QAM modulated signal.

IV. Conclusion

In this paper, an ultra-wideband, high-efficiency class-E PA operating across four frequency bands is presented. The PA demonstrates a 3 dB small-signal BW of 138% (6–32.5 GHz) and a 1 dB large-signal power BW of 132% (7–34 GHz). At 14 GHz, the $\mathrm{P_{SAT}}$ reaches 19.2 dBm and the $\mathrm{OP_{1dB}}$ remains >16 dBm across 8–32 GHz. At 28 GHz, the PA achieves a peak PAE of 34% while maintaining >28% from 8 to 31 GHz, validating the effectiveness of the class-E OLN. Under a single-carrier 400 MHz 64-QAM DFT-s-OFDM modulation at 28 GHz, the PA delivers a $\mathrm{P_{avg}/PAE_{avg}}$ of 15.5 dBm/16.3% with excellent ACLRs $\leq$-34.4 dBc and an EVM of -28.6 dB. To the best of the authors' knowledge, this multiband class-E PA achieves the widest BW with excellent FoM, PAE, and linearity performance among previously published state-of-the-art silicon-based wideband PAs.

Acknowledgment

The authors would like to thank Keysight Technologies in Böblingen, Germany for assistance with calibration and setup of modulation distortion (EVM/ACLR) measurements.

References

[1] A. Piacibello, R. Giofré, R. Quaglia, and V. Camarchia, "34 dBm GaN Doherty power amplifier for Ka-band satellite downlink," in *15th Eur. Microw. Integr. Circuits Conf. (EuMIC)*, Utrecht, Netherlands, Jan. 2021, pp. 25–28.

[2] R. Giofrè *et al.*, "A 17.3–20.2-GHz GaN-Si MMIC balanced HPA for very high throughput satellites," *IEEE Microw. Wirel. Compon. Lett.*, vol. 31, no. 3, pp. 296–299, 2021.

[3] O. Kazan, Z. Hu, L. Li, A. Alhamed, and G. M. Rebeiz, "An 8-channel 5–33-GHz transmit phased array beamforming IC with 10.8–14.7-dBm Psat for C-, X-, Ku-, and Ka-band SATCOM," *IEEE Trans. Microw. Theory Techn.*, vol. 71, no. 5, pp. 2029–2039, 2023.

[4] K. Ding *et al.*, "A 23 GHz RF-beamforming transmitter with >15.5 dBm $\mathrm{P_{sat}}$ and >21.7% peak efficiency for inter-satellite communications," in *IEEE Radio Freq. Integr. Circuits Symp. Dig. Tech. Pap. (RFIC)*, Denver, CO, USA, Jun. 2022, pp. 103–106.

[5] N. R. S. Alluri and P. Asbeck, "A Ka band 2-stage linear Doherty amplifier with 23dBm Psat and 29% 6dB-backoff PAE in pMOS-SOI," in *IEEE Topical Conf. on RF/Microw. Power Amplifiers for Radio and Wirel. Applications (PAWR)*, San Diego, CA, USA, Jan. 2021, pp. 52–54.

[6] A. Grebennikov, "High-efficiency class-E power amplifier with shunt capacitance and shunt filter," *IEEE Trans. Circuits Syst. I: Regular Papers*, vol. 63, no. 1, pp. 12–22, Jan. 2016.

[7] M. Schröter and A. Chakravorty, *Compact hierarchical modeling of bipolar transistors with HICUM*. Singapore: World Scientific, 2010.

[8] Y.-W. Chang *et al.*, "A 28 GHz linear and efficient power amplifier supporting wideband OFDM for 5G in 28nm CMOS," in *IEEE/MTT-S Int. Microw. Symp. (IMS)*, Los Angeles, CA, USA, Aug. 2020, pp. 1093–1096.

[9] T.-W. Li, M.-Y. Huang, and H. Wang, "Millimeter-wave continuous-mode power amplifier for 5G MIMO applications," *IEEE Trans. Microw. Theory Techn.*, vol. 67, no. 7, pp. 3088–3098, Jul. 2019.

[10] T. Kim, H. Jeong, S. Jang, J. Lee, and C. Park, "Ka-Band CMOS power amplifier using stacked structure with cascode-like operation," *IEEE Trans. Circuits Syst. II: Express Briefs*, vol. 71, no. 4, pp. 1949–1953, Apr. 2024.

[11] T.-C. Tsai *et al.*, "A linear and efficient power amplifier supporting wideband 64-QAM for 5G applications from 26 to 30 GHz in SiGe:C BiCMOS," in *IEEE Radio Freq. Integr. Circuits Symp. (RFIC)*, Atlanta, GA, USA, Jun. 2021, pp. 127–130.

[12] H. Lee, I. Han, and I. Ju, "A highly efficient, linear Ka-band SiGe HBT cascode power amplifier with a compact lumped element coupled line impedance inverting balun," *IEEE Trans. Microw. Theory Techn.*, vol. 72, no. 10, pp. 5799–5808, Oct. 2024.